

Communications

Designing Various Self-Assembled ZnO_x Quantum Dots/Islands on Silicon with Distinctive Characteristics by Magnetron Sputter

Yu-Han Liang, Jun-Han Huang, Neng-Chieh Chang, and Chuan-Pu Liu*

Department of Materials Science and Engineering, National Cheng-Kung University, No. 1, University Road, Tainan 701, Taiwan

Received December 24, 2008; Revised Manuscript Received February 16, 2009

ABSTRACT: Three types of self-assembled ZnO_x quantum dots (QDs) or islands on silicon substrates with distinctive morphologies were successfully synthesized using various growth schemes in a simple magnetron sputter. If hydrogen/argon was employed as the sputtering gas under negative substrate bias, the growth started from surface pit formation, leading to self-aligned cone shaped ZnO_x QDs with composition, *x*, being linearly dependent on substrate bias, providing an ideal platform for defect engineering and related application. Intriguingly, if there is no substrate bias applied, the most energetically favorable ZnO_x hexagonal pyramids were formed on the surface, in quasi-epitaxy with the Si substrate. Spherical stoichiometric ZnO QDs in a narrow size range were synthesized when oxygen was particularly introduced, and these exhibited true quantum confinement effects, evidenced by a blue shift of the UV emission in the photoluminescence spectrum. This work facilitates the development of controllable ZnO QDs, and, most importantly, sheds light on the quick implantation of ZnO QDs into devices by an industrially compatible sputter.

Because of the extreme confinement effects, semiconductor quantum dots (QDs) of three-dimensional confined structures represent the lowest dimensional nano-objects and provide a good platform for studying new physical phenomena in mesoscopic physics, from which many new nanodevices have been realized. In the fabrication of QDs, although significant progress has been made for group V and III–V semiconductors,^{1,2} fabricating epitaxial ZnO QDs still remains a serious challenge. ZnO is a direct wide band gap material of 3.37 eV at room temperature and possesses larger exciton binding energy of 60 meV when compared with other semiconductor counterparts, such as GaN (21–25 meV) and ZnSe (22 meV).³ Recently, one-dimensional ZnO nanostructures with high quality have been synthesized fairly easily by various methods,⁴ probably because of the high anisotropic properties of their surface energy. Consequently, ZnO has been used with various types of impurities in the development of functional nanodevices, such as optoelectronics,⁵ information storage devices,⁶ sensors,⁷ and solar cells.⁸ However, ZnO nanodevices utilizing quantum confinement effects are difficult to achieve, because the exciton Bohr radius of ZnO is only 1.8 nm, which is much smaller than that of other semiconductor materials. Thus, more work into fabricating ZnO QDs with true quantum confinement is required. Various methods have been employed to prepare solid-state ZnO QDs, most of which are based on physical techniques, such as vapor phase transport process,⁹ pulsed laser deposition,¹⁰ metal-organic chemical vapor deposition,^{11,12} and molecular beam epitaxy via the self-assembly Stranski-Krastanov growth mode.^{13,14} However, the as-synthesized QDs from these methods are still far from ideal, with the main problem being poor crystal quality. Most seriously,

UV luminescence in the as-prepared ZnO QDs is often quenched, whereas low-energy defect-induced emission commonly dominates the photoluminescence (PL) spectrum unless additional surface modification or postdeposition annealing treatments are performed. Thus, growing solid-state ZnO quantum dots with good quality appears to be very challenging. Moreover, the methods listed above are time-consuming and expensive with harsh conditions, which prevent them from being used for large-scale production and in wide applications. Therefore, the primary breakthrough of this work is to provide a feasible and reliable method to fabricate high-quality self-assembled ZnO QDs/islands uniformly over a large area on Si by RF magnetron sputtering through a unique design in the growth scheme. There are three different types of low-dimensional QDs/islands fabricated in this study, each with a distinctive shape and composition for different device applications. The control over size, shape, and composition offered by this technique is superior to that of any of the methods investigated so far.

Experimental Section. Synthesis of ZnO_x Quantum Dots/Islands. All experimental processes were conducted only by RF magnetron sputtering with different silicon substrate, working gas, and substrate bias at a base pressure of 3.0×10^{-6} Torr. In this work, high purity (99.99%) polycrystalline ZnO was used as a target during the sputtering process. All types of QDs/islands were grown uniformly on 4 in. silicon wafers at an elevated temperature of 400 °C.

Characterization. The morphology and structure of the as-synthesized QDs/islands were characterized by field-emission scanning electron microscopy (FE-SEM 7000F) and high-resolution transmission electron microscopy (TEM). TEM images, high-resolution images (HRTEM), and electron diffraction patterns were obtained on a JEOL2100F microscope operating at an accelerating

* Corresponding author. E-mail: cpliu@mail.ncku.edu.tw.

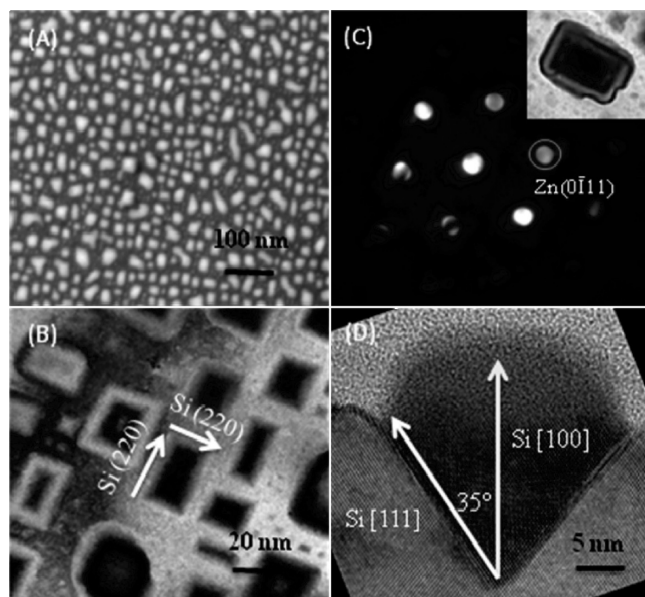


Figure 1. (A) SEM image, and (B) plan-view bright-field TEM image along Si [001] of the imbedded cone shaped ZnO_x QDs on Si (001), along with (C) diffraction pattern and (D) high-resolution TEM image of a typical QD.

voltage of 200 keV. The compositions and properties of the QDs/islands produced were analyzed by Raman spectroscopy carried out using a Labram HR micro PL-Raman. Room temperature photoluminescence (PL) spectra were recorded using a 325 nm line from a He–Cd laser as the excitation source.

Results and Discussion. The first type of QDs is embedded cone shaped dots, which were synthesized on silicon (100) wafer using pure Ar as a working gas under negative substrate bias at an elevated temperature of 400 °C during sputtering. The low-magnification SEM image in Figure 1A shows a typical sample synthesized under the substrate bias of −400 V for the growth time of 30 min, where the as-prepared high-density QDs are estimated to be $2.3 \times 10^{11}/\text{cm}^2$, with the average dot size of 20 nm, uniformly distributed on the substrate. In general, the dot size is proportional to both substrate bias and growth time until saturation at about 30 nm for the limiting substrate bias or growth time, whereas the dot shape remains the same. Furthermore, the microstructure of the as-prepared QDs was characterized by TEM to examine the growth mechanisms. The results of the sample from Figure 1A are shown in images B, C, and D in Figure 1, where Figure 1B shows a plan-view bright-field image under Si 001 zone axis, whereas images C and D in Figure 1 show a diffraction pattern and HRTEM cross-sectional image of a single dot under the Si 110 zone axis. Figure 1B reveals the dots take square or rectangular shape, highly ordered along the Si [220] direction, by comparing the image to the diffraction pattern (not shown). Most importantly, all dots exhibit black and white fringes along the four major 220 directions, indicating they are coherent or at least semicoherent dots with Si and undergo elastic relaxation toward the tops of the dots. The high perfection of the crystallinity of the dots is evidenced by the diffraction pattern of a typical dot in Figure 1C. However the most striking feature from Figure 1D is that the growth of the dots started from the surface pits, which were not present before sputtering, forming embedded cone-shaped QDs. Figure 1D reveals that the exposed sidewalls of the QDs are inclined at 35° to the Si [001], corresponding to the Si (111) facets. The silicon etching pits have been shown to be formed by plasma etching¹⁵ because of the ultrahigh substrate bias applied on the Si substrate leading to a huge amount of energetic ionized Ar⁺, accelerated by the negative substrate bias, bombarding the silicon substrate. In addition, the sputtering yield is highly dependent on crystallography, where the

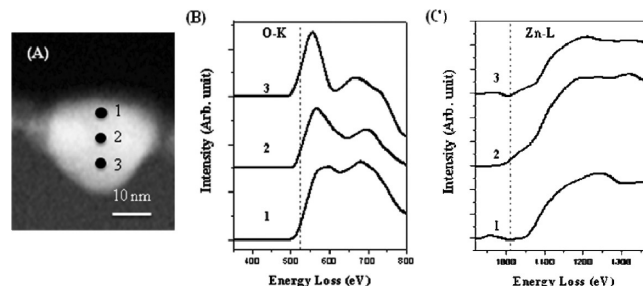


Figure 2. (A) STEM-HAADF image of a single cone-shaped quantum dot, with EELS spectra of (B) the O–K edge and (C) the Zn–L edge acquired from positions 1 to 3 in A.

Table 1. Composition of Zn and O for Positions 1–3 As Marked in Figure 2A Calculated from the STEM-EELS Spectra B and C in Figure 2

analysis no.	[Zn] (at %)	[O] (at %)
1	52.54	47.46
2	85.10	14.90
3	95.67	4.33

bonding energy of the silicon surface is found to be: (111) > (110) > (100);¹⁶ therefore, the remaining Si (111) surface can be observed because Si {111} has a relative lower etching rate than any of the other silicon facets.

The composition of the as-synthesized QDs was characterized by electron energy loss spectroscopy (EELS) with scanning TEM (STEM), which is shown in Figure 2. Figure 2A shows the high-angle annular dark-field image of a typical cone shaped dot, exhibiting brighter contrast than the Si substrate. EELS spectra acquired from positions 1 to 3 as marked in Figure 2A, representing the dot surface to dot center, are shown in Figure 2B for the O–K edge at 532 eV and in Figure 2C for the Zn–L edge at 1020 eV. The elemental ratio of oxygen to zinc can be quantified from panels B and C in Figure 2, and is summarized in Table 1. The results indicate that oxygen concentration gradually decreases with the depth into the dot center. As a result, the core of a dot is mainly composed of Zn, and the ZnO_x shell is formed during later growth. Interestingly, through a systematic study, it is found that the ratio of oxygen to zinc in the core is a linear function of applied substrate bias, which can be varied from pure zinc to close to stoichiometry while retaining the same shape. Consequently, we propose that the cone shaped dots are a result of dynamic equilibrium between the deposition of ZnO_x and the resputtering of ZnO_x and Si. The energetic Ar⁺ ions supplied by the substrate bias can easily break Zn–O bonding, since the bonding energy of Zn–O is ~3 eV,¹⁷ mostly leaving behind metal Zn, which is liquid at the growth temperature. This may be the reason why the dynamic equilibrium can be established. The liquid metal droplet formation can be clearly confirmed by another parallel deposition experiment on a Si (111) substrate under identical growth conditions, where no surface pits were formed during sputtering (please see Figure S1A and S1B in the Supporting Information for SEM plan-view and cross-sectional HRTEM image, respectively). The droplets were not confined in the surface pits, and thus exhibit irregular shape.

To synthesize stoichiometric ZnO QDs, we employed a mixed gas of 40% O₂ and 60% Ar as the working gas to replenish the oxygen-deficient QDs during the reactive sputtering process to form the second type of QDs. With more oxygen flux in the chamber, we can expect that the deposited molecules tend to be ZnO_x. As an example, the SEM image in Figure 3A shows that the as-grown QDs under the substrate bias of −300 V are spherical in shape and much smaller than those grown with Ar plasma, in a narrow size range of 4.2–6.8 nm, with the density of the dots estimated to be $2 \times 10^{12}/\text{cm}^2$. The cross-sectional TEM bright-field image in Figure 3B and the HRTEM image in the inset reveal that the QDs are

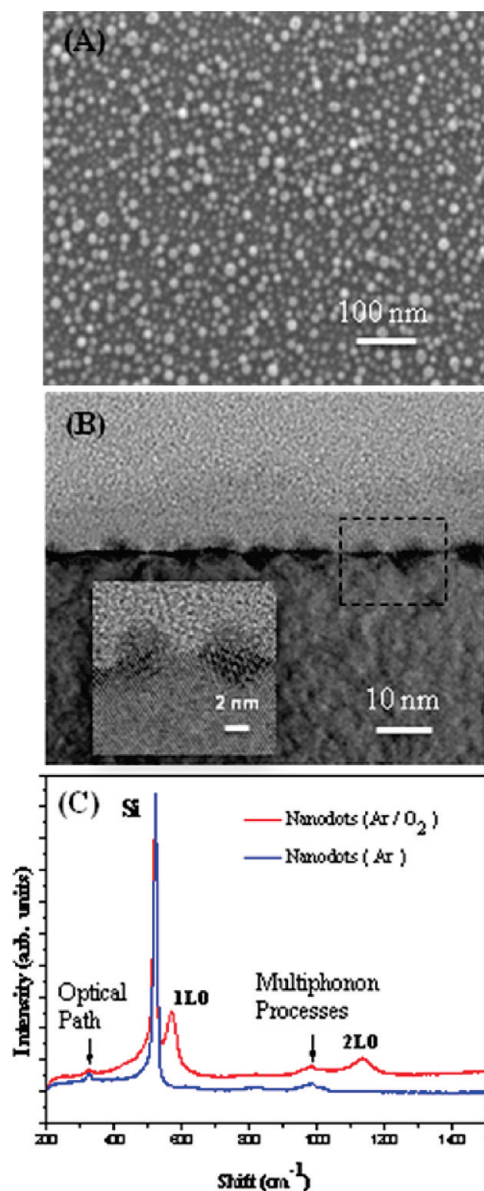


Figure 3. (A) SEM image of the as-synthesized QDs grown with an Ar/O₂ working atmosphere. (B) Cross-sectional TEM bright-field image of the QDs with the insert showing the corresponding high-resolution TEM image. (C) Raman spectra of the QDs grown with Ar and Ar/O₂ atm.

single crystalline with a size of 5 nm and a high aspect ratio of about one, with some of them also nucleated from tiny surface pits. Under this sputtering condition, the sputtered species is solid ZnO rather than metal liquid Zn clusters, which could fill up the tiny surface pits formed in the very beginning and block further bombardment or even faster nucleation on regions with no pits. Owing to the shorter diffusion length of ZnO_x molecules compared to the metal Zn in the first case, the spherical dots are smaller than cone-shaped QDs.

Raman spectra of ZnO QDs grown with Ar/O₂ atmosphere under 325 nm excitation in Figure 3C show that the first-order longitudinal-optical (LO) peak resulting from A₁ polar symmetry is centered at 570 nm⁻¹, compared with 574 cm⁻¹ of ZnO bulk.¹⁸ In contrast, the spectrum of the cone shaped QDs shows no ZnO A₁ (LO) phonon mode, providing further evidence that Zn makes up most of the cores again. Fonoberov and Balandin predicted¹⁹ from a theoretical calculation that the confined polar optical phonons in wurtzite QDs would show a discrete spectrum of frequencies different from those of the bulk crystal. In our case, the average quantum dot size of around 5 nm is comparable to the exciton Bohr

radius of bulk ZnO (2.34 nm).²⁰ Rajalakshmi et al. have reported the optical phonon confinement in ZnO nanoparticles,²¹ which also leads to red-shifted optical phonons in the Raman spectra. Alim et al. reported a red-shifted A₁ (LO) phonon peak at 570 cm⁻¹ from 20 nm ZnO QDs.²² However, the peak of 984 cm⁻¹, observed between the first- (1LO) and the second-order (2LO) phonon peaks, is attributed to the multiphonon processes that presumably occur for phonon wave vectors away from the center of the Brillouin zone.²³

To further improve the crystallinity without incurring serious adverse effects from ion bombardment for the microstructure and composition, we employed a hydrogen ambient during sputtering. Consequently, the most intriguing and well-faceted type of ZnO_x pyramidal islands were obtained. The role of hydrogen in the growth and properties of ZnO has been investigated by Sano et al.,²⁴ and their results indicated that the crystallinity of ZnO_x can be improved because of the enhancement of surface diffusion of adatoms under hydrogen irradiation and the electron mobility can be increased significantly by the hydrogen treatment. The typical morphology of the dots is shown in Figure 4A, which were deposited using a mixed gas of 20% H₂ and 80% Ar as the working gas on a Si (111) substrate at 400 °C without any substrate bias applied for the growth time of 30 min, shows that the ZnO hexagonal pyramids roughly range from 60 to 120 nm in base length, and the density of the pyramids is estimated to be around $1.2 \times 10^8/\text{cm}^2$. This suggests that the adatoms with high surface mobility result in long migration length originating from both high growth temperature and termination of the surface with hydrogen atoms.²³ The pyramids exhibit only two specific orientations on Si (111), as indicated in the plan-view TEM bright-field image of Figure 4B. According to the diffraction pattern in Figure 4C, the pyramids are aligned with Si [111] substrate as Si [111]//ZnO [0001] and Si [220]//ZnO [1010]. Therefore, the ZnO_x pyramids exhibit rotational symmetry, positioned 30° to each other on the substrate surface. The cross-sectional SEM image in Figure 4D reveals that each side plane subtends to 64°, which is consistent with the atomic model in equilibrium proposed by Zhou et al.,²⁵ as illustrated in the insert of Figure 4D. This growth method achieves the most stable ZnO_x pyramidal shaped nanocrystals constructed by the basal polar (0001) plane with O-terminals and the side polar {1011} planes with O-terminals, which can be verified by the cross-sectional TEM bright-field image with diffraction patterns in Figure 4E. The maximum crystal growth velocity of the wurzite structure is along the (0001) direction by following the relationship: [0001] > [1011] > [1010]. During crystal growth, the polar {0001} surfaces usually appear as growing surfaces because of their high surface energy, and present small facets or even disappear. On the other hand, another possible mechanism for the formation of {1011} facets on the ZnO_x pyramids is due to the lower hydrogen etching than for other facets. The HRTEM image of the interface in Figure 4F shows that the pyramid is a wurzite structure with the lattice spacing of 0.26 nm for the basal planes and a native oxide layer of about 2 nm is present without any wetting layer. The X-ray energy dispersive spectrum (EDS) in Figure 4G confirms that the as-synthesized pyramids are composed of ZnO_x, which demonstrates that the hydrogen in the hydrogen-containing plasma also contributed to the reduction reaction during the sputtering process.²⁶

Figure 5 shows the room-temperature PL spectra of the as-grown imbedded cone ZnO QDs from Figure 1A, the spherical ZnO QDs from Figure 3A, and the ZnO_x hexagonal pyramids from Figure 4A. For the ZnO_x pyramids, the near band edge excitonic emission is observed at 3.35 eV, which is somewhat blue-shifted from the UV band emission in ZnO bulk crystals or thin films at room temperature, probably related to the residual strain from the lattice mismatch. It can thus be attested that high-quality ZnO QDs can be formed only by utilizing RF magnetron sputtering. Because of

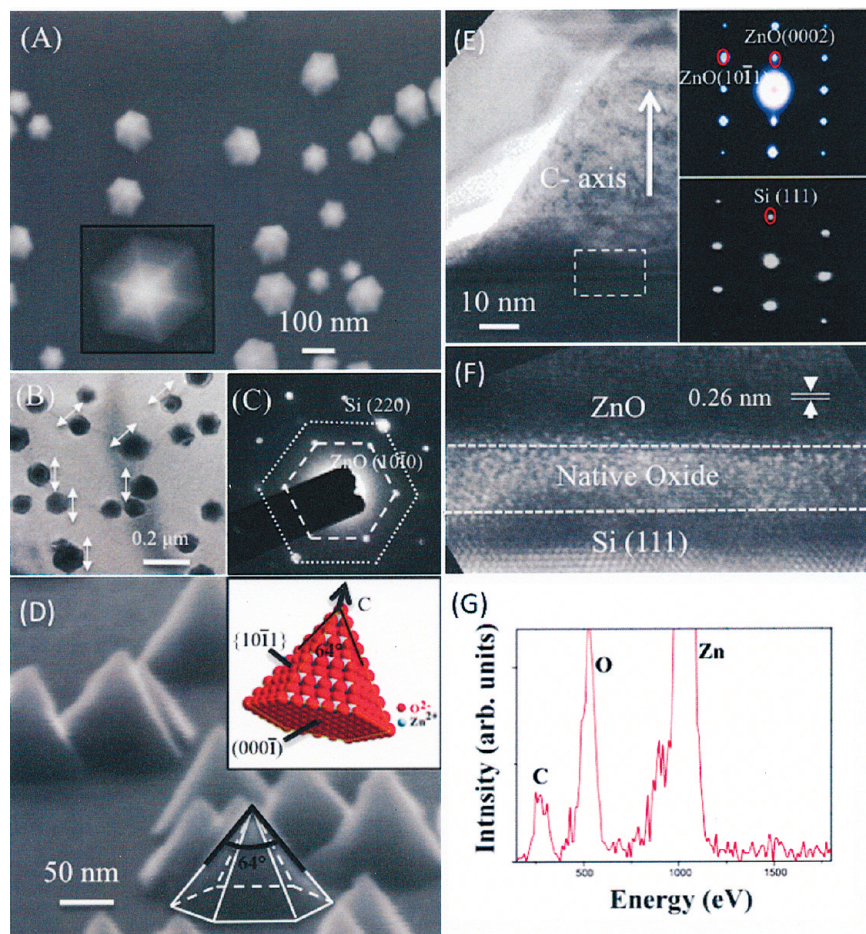


Figure 4. (A) SEM image of the as-prepared ZnO_x hexagonal pyramids grown on a Si (111) substrate with an enlarged SEM image in the inset. (B) Plan-view bright-field image of the ZnO_x pyramids. (C) Diffraction pattern of the ZnO pyramids with silicon substrate showing that Si [220]/ZnO [1010]. (D) Cross-sectional SEM image of ZnO_x pyramids with an ideal ZnO crystal model shown in the inset.²⁴ (E) Cross-sectional TEM image of the ZnO_x hexagonal pyramid with the diffraction patterns. (F) HRTEM image of the interface. (G) STEM-EDS spectra of a ZnO_x pyramid.

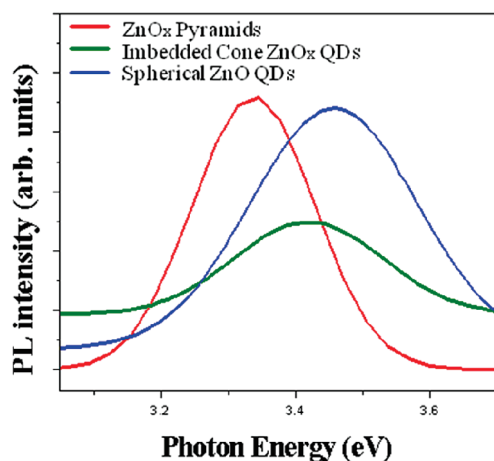


Figure 5. Room-temperature PL spectra of imbedded cone ZnO_x QDs and spherical ZnO QDs grown with H₂/Ar and O₂/Ar, respectively, and of ZnO_x pyramids grown with a H₂/Ar atmosphere, using a He–Cd laser as the excitation source at a wavelength of 325 nm.

the presence of zinc in the core of the cone-shaped ZnO_x QDs, the integrated intensity is much weaker than that of the other two types of islands. Besides, intriguingly the UV band emission is blue-shifted to 3.42 eV, clearly related to the ZnO shell structures. However, complete understanding of the emission mechanism requires comprehensive analysis on the complicated variations of

composition and shape involved. As for the ZnO spherical QDs, the UV peak is located at an even higher photon energy of 3.46 eV, and this conspicuous blue shift may be due to the size effect. In general, quantum confinement shifts the energy levels of the conduction and valence bands apart, giving rise to a blue shift in the transition energy as the size of QDs decreases. Because the dimension of the ZnO dots is larger than the ZnO excitonic Bohr radius, the center of mass motion of excitons is thus quantized by the confinement potential and the relative carrier motion is dominated by Coulomb interactions. This is a so-called weak confinement, written as²⁷

$$E_g = E_g^{\text{bulk}} + \frac{\hbar^2 \pi^2}{2er^2} \left(\frac{1}{m_e} + \frac{1}{m_h} \right) - \frac{1.8e^2}{4\pi\epsilon\epsilon_0 r} \quad (1)$$

where E_g^{bulk} is the bulk energy gap (3.37 eV), r is the average radius of spherical particles, e is the charge of the electron, and \hbar is the Dirac's constant, whereas ϵ_0 is the permittivity of free space and ϵ_0 is the relative permittivity. The electron and hole effective masses in ZnO are taken as $m_e = 0.24m_0$ and $m_h = 0.45m_0$, respectively. The polarization term in this model is usually negligible. If the average diameter of the ZnO QDs is taken to be 5 nm from Figure 3B, the calculated band gap is 3.47 eV, which agrees well with the experimental data. In addition, the strain-induced band gap shift also needs to be considered, because the smallest lattice mismatch between the Zn (1000) and Si (111) is still as high as 18%.²⁸ The residual stress due to a large lattice mismatch between ZnO and Si can also partially contribute to the blue shift.

Conclusion. In summary, versatile ZnO_x QDs, including imbedded cone ZnO_x , spherical ZnO QDs, and pyramidal ZnO_x islands, were synthesized by RF magnetron sputtering through controlling the substrate bias, working gas, and silicon substrate. The composition and morphology of the QDs/islands can be varied systematically and reliably over a certain range, and thus the optical properties can be varied accordingly. This unique technique can provide the advantages of high density, uniformity, and size for quantum dots fabrication on a large scale, and so has great potential to be applied for industrial applications.

Acknowledgment. This work has been supported by the National Science Council of Taiwan (Grants NSC95–2221-E-006–079-MY3 and NSC95–2221-E-006–080-MY3).

Supporting Information Available: SEM and HRTEM images of Zn droplets (PDF). This material is available free of charge via the Internet at <http://pubs.acs.org>.

References

- (1) Asahi, H. *Adv. Mater.* **1997**, *9*, 1019–1026.
- (2) Liu, D. C.; Lee, C. P. U.S. Patent 5 482 890, 1996.
- (3) Tan, S. T.; Sun, X. W.; Zhang, X. H. *J. Cryst. Growth* **2006**, *290*, 518–522.
- (4) Liu, C. P.; Wang, R. C.; Kuo, C. L.; Liang, Y. H.; Chen, W. Y. *Recent Pat. Nanotechnol.* **2007**, *1*, 11–20.
- (5) Vispute, R. D.; Talyansky, V.; Chooon, S.; Sharma, R. P.; Venkatesan, T.; He, M.; Tang, X.; Halpern, J. B.; Spencer, M. G.; Li, Y. X.; Salamanca-Riba, L. G.; Iliadis, A. A.; Jones, K. A. *Appl. Phys. Lett.* **1998**, *73*, 348–350.
- (6) Botello-Mendez, A. R.; Lopez-Urias, F.; Terrones, M.; Terrones, H. *Nano Lett.* **2008**, *8*, 1562–1565.
- (7) Wang, X.; Zhou, J.; Song, J.; Liu, J.; Xu, N.; Wang, Z. L. *Nano Lett.* **2006**, *6*, 2768–2772.
- (8) Leschkies, K. S.; Divakar, R.; Basu, J.; Enache-Pommer, E.; Boercker, J. E.; Carter, C. B.; Kortshagen, U. R.; Norris, D. J.; Aydil, E. S. *Nano Lett.* **2007**, *7*, 1793–1798.
- (9) Lu, J. G.; Ye, Z. Z.; Huang, J. Y.; Zhu, L. P.; Zhao, B. H. *Appl. Phys. Lett.* **2006**, *88*, 063110–1063110–3.
- (10) Bae, C. H.; Park, S. M.; Park, S. C.; Ha, J. S. *Nanotechnology* **2006**, *17*, 381–384.
- (11) Nakamura, A.; Okamatsu, K.; Tawara, T.; Gotoh, H.; Temmyo, J.; Matsui, Y. *Jpn. J. Appl. Phys.* **2008**, *47*, 3007–3009.
- (12) Kim, S. W.; Fujita, S.; Fujita, S. *Appl. Phys. Lett.* **2002**, *81*, 5036–5038.
- (13) Gong, Q.; Offermans, P.; Nötzel, R.; Koenraad, P. M.; Wolter, J. H. *Appl. Phys. Lett.* **2004**, *85*, 5697–5699.
- (14) Chen, Y.; Zhu, Z.; Bagnall, D. M. *J. Cryst. Growth* **1998**, *184*–185, 269–273.
- (15) Labanda, J. G. C.; Barnett, S. A.; Hultman, L. *J. Vac. Sci. Technol., B* **1998**, *16*, 1885–1998.
- (16) Jiang, Y.; Huang, Q. A. *Semicond. Sci. Technol.* **2005**, *20*, 524–531.
- (17) Chapman, B. In *Glow Discharge Processes*; Wiley: New York, 1980.
- (18) Ashkenov, N.; Mbenkum, B. N.; Bundesmann, C.; Riede, V.; Lorenz, M.; Spemann, D.; Kaidashev, E. M.; Kasic, A.; Schubert, M.; Grundmann, M.; Wagner, G.; Neumann, H.; Darakchieva, V.; Arwin, H.; Monemar, B. *J. Appl. Phys.* **2003**, *93*, 126–133.
- (19) Fonoberov, V. A.; Balandin, A. A. *Phys. Rev. B* **2004**, *70*, 233205–233209.
- (20) Senger, R. T.; Bajaj, K. K. *Phys. Rev. B* **2003**, *68*, 045313–045321.
- (21) Rajalakshmi, M.; Arora, A. K.; Bendre, B. S.; Mahamuni, S. *J. Appl. Phys.* **2000**, *87*, 2445–2448.
- (22) Alim, K. A.; Fonoberov, V. A.; Shamsa, M.; Balandin, A. A. *J. Appl. Phys.* **2005**, *97*, 124313–1124313–5.
- (23) Damen, T. C.; Porto, S. P. S.; Tell, B. *Phys. Rev.* **1966**, *142*, 570–574.
- (24) Sano, M.; Miyamoto, K.; Kato, H.; Yao, T. *J. Appl. Phys.* **2004**, *95*, 5527–5531.
- (25) Zhou, X.; Xie, Z. X.; Jiang, Z. Y.; Kuang, Q.; Zhang, S. H.; Xu, T.; Huang, R. B.; Zheng, L. S. *Chem. Commun.* **2005**, *44*, 5572–5574.
- (26) Exarhos, G. J.; Rose, A.; Windisch, C. F., Jr. *Thin Solid Films* **1997**, *308*–309, 56–62.
- (27) Brus, L. E. *J. Chem. Phys.* **1984**, *80*, 4403–4407.
- (28) Rickerby, D. S.; Matthews, A. In *Advanced Surface Coatings: A Handbook of Engineering*; Chapman and Hall: New York, 1991; Vol. 94.

CG8014018